Available online at www.sciencedirect.com

SciVerse ScienceDirect

Acta Materialia 60 (2012) 5984–5999

Acta MATERIALIA

www.elsevier.com/locate/actamat

Linking phase-field and finite-element modeling for process–structure–property relations of a Ni-base superalloy

Bradley S. Fromm [a,*], Kunok Chang [b], David L. McDowell [a,c], Long-Qing Chen [b], Hamid Garmestani [a]

[a] School of Materials Science and Engineering, Georgia Institute of Technology, Atlanta, GA 30332, USA
[b] Department of Materials Science and Engineering, The Pennsylvania State University, University Park, PA 16802, USA
[c] The George W. Woodruff School of Mechanical Engineering, Georgia Institute of Technology, Atlanta, GA 30332, USA

Received 18 April 2012; received in revised form 25 June 2012; accepted 29 June 2012
Available online 30 August 2012

Abstract

Establishing process–structure–property relationships is an important objective in the paradigm of materials design in order to reduce the time and cost needed to develop new materials. A method to link phase-field (process–structure relations) and microstructure-sensitive finite-element (structure–property relations) modeling is demonstrated for subsolvus polycrystalline IN100. A three-dimensional experimental dataset obtained by orientation imaging microscopy performed on serial sections is utilized to calibrate a phase-field model and to calculate inputs for a finite-element analysis. Simulated annealing of the dataset realized through phase-field modeling results in a range of coarsened microstructures with varying grain size distributions that are each input into the finite-element model. A rate-dependent crystal plasticity constitutive model that captures the first-order effects of grain size, precipitate size and precipitate volume fraction on the mechanical response of IN100 at 650 °C is used to simulate stress–strain behavior of the coarsened polycrystals. Model limitations and ideas for future work are discussed.

Keywords: Finite-element method; Crystal plasticity; Phase-field modeling; Process–structure–property relations; Microstructure-sensitive design

1. Introduction

Establishing process–structure–property relationships is essential in leveraging modeling and simulation to reduce the time and cost needed to develop new materials or improve existing materials [1,2] and is at the core of materials design. Fig. 1 illustrates how the process–structure–property relationships form overlapping regions that represent physical couplings and transfer of related model information in materials design. Just as a material's microstructure is coupled to the process path, its mechanical properties are directly correlated to the material microstructure.

Substantial progress has been made in connecting the process–structure–property relationships through advances in computational materials science and materials characterization methods. For example, continuum mechanics-based techniques such as phase-field modeling (PFM) enable a direct linkage between the process–structure relationships by simulating the nucleation and growth of phases/grains within a material [3,4]. Likewise, microstructure-sensitive finite-element modeling (FEM) facilitates the structure–property correlation by predicting the anisotropic mechanical response of materials under thermomechanical loading conditions, including the role of mesoscopic microstructure morphology (e.g. grains, phases) [5–7]. Further advances in characterization techniques such as automated electron backscatter diffraction (EBSD) methods [8–10] and three-dimensional (3-D) X-ray diffraction [11,12] allow for digital representation of polycrystalline microstructures and facilitate calibration of the computational models.

* Corresponding author.
E-mail address: bfromm3@gatech.edu (B.S. Fromm).

1359-6454/$36.00
http://dx.doi.org/10.1016/j.actamat.2012.06.058

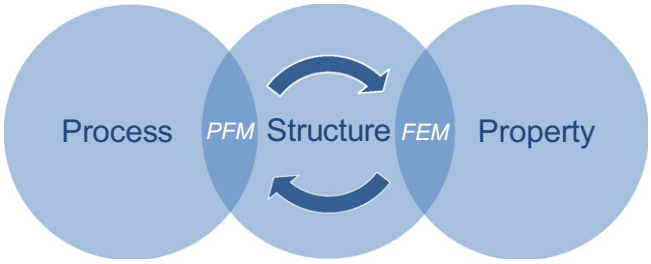

Fig. 1. Developing linkages between phase-field and finite-element models facilitate process–structure–property predictions that are at the core of materials design. The two-way connection between process–structure and structure–property relations enables the development of top-down material design strategies.

Due to the time and cost required to develop new materials, there is considerable incentive to apply computational materials science approaches such as PFM and FEM to the materials design and development process. A long-term goal within the materials community is the development of materials design methods that permit top-down assessment of the process–structure–property relations based on bottom-up modeling and characterization at various scales. This type of methodology will enable designers to tailor materials that are optimized for specific applications. An important step towards achieving these goals is to develop a two-way coupling between PFM and FEM modeling techniques, as depicted in Fig. 1. Such a coupling will allow for the exchange of key parameters between the models. For example, values of dislocation density from the PFM can be transferred to the FEM to enable more accurate calculation of local stress and strain. Conversely, updated values of crystallographic orientation, position, or elastic strain obtained from the FEM can be conveyed back to the PFM to improve predictions of microstructure evolution. For the present work, only a one-way coupling is needed to predict mechanical response. However, future work to establish top-down design procedures will require the use of a bidirectional linkage.

The purpose of this paper is to link PFM and FEM to establish an interface between process–structure and structure–property relations. The approach is demonstrated for a powder metallurgy-processed Ni-base superalloy, IN100, utilizing a 3-D microstructure characterized experimentally through EBSD performed on serial sections to serve primarily as input into PFM simulations. Various microstructures obtained through the simulated annealing (coarsening) of the dataset based on application of the PFM are input into a microstructure-sensitive crystal plasticity formulation to predict the stress–strain response as a function of successively increasing mean grain size.

2. Methodology

2.1. Phase-field model

Grain growth of polycrystalline materials can be modeled using the phase-field method. Both nucleation and growth of grains can be considered. The PFM approach described here is based on the work of Chen and Yang [3], who utilized a set of non-conserved order parameters to represent crystallographic texture (crystallographic orientation of each grain) within the model. Chen and associates have successfully applied PFM to both 2-D [13–15] and 3-D problems [4,15,16].

The PFM used in this study is summarized in Table 1. A 3-D formulation is employed wherein the polycrystalline grain structure is represented by a set of Q-order parameters $\{(\eta_1(\boldsymbol{r},t),\eta_2(\boldsymbol{r},t),\ldots,\eta_Q(\boldsymbol{r},t)\}$ representing grain orientation, with $\boldsymbol{r}$ defining the spatial position, t the simulation time, and Q the number of grains in the simulation. Grain boundary evolution is described by solving the time-dependent Ginzburg–Landau equations for each order parameter, as shown in Eq. (1).

Here L_i are grain boundary mobility coefficients, $F(t)$ represents the total free energy of the microstructure, and f_o is known as the local free energy density. The κ_i in Eq. (2) are positive-valued gradient energy coefficients. For local free energy parameters that satisfy the conditions $\alpha=\beta$, $\gamma>\alpha/2$, and for α, β, and $\gamma>0$, the local free energy in Eq. (3) satisfies minima at $(\eta_1,\eta_2,\eta_Q)=(\pm1,0,0)$, and $(0,\pm1,\ldots,0)$, and $(0,0,\ldots,\pm1)$. Recent work by Svoboda et al. [17] has demonstrated the equivalence of the time-dependent Ginzburg–Landau PFM approach to grain boundary migration with the thermodynamic extremal principle (TEP) of maximum dissipation for processes assumed to follow linearized non-equilibrium kinetics (thermodynamics force–flux relations). The TEP has been applied by Svoboda and Fischer [18] to coarsening of distributions of precipitates in multicomponent systems as well.

Substituting Eqs. (2) and (3) into (1) and simplifying yields the grain growth evolution equation found in Eq. (4). A forward Euler scheme in Eq. (5) is used to solve the time-dependent partial different equation. To avoid aphysical coalescence of the grains which mainly takes place during the early stage of the simulation, to reduce simulation time, and to minimize memory usage, the active parameter tracking (APT) algorithm of Vedantam and Patnaik [19] is applied such that the evolution equations are solved for only the active order parameters corresponding to grain boundary regions. A more in-depth discussion of PFM can be found in the cited literature. PFM results are presented in Section 4.

2.2. Microstructure-sensitive finite-element model

Ni-base superalloys are used in high-temperature applications requiring high strength, excellent damage tolerance and long-term creep resistance. Their yield strength at elevated temperature stems from the coherent dispersion of Ni_3Al precipitates within the face-centered cubic (fcc) solution-strengthened Ni matrix that provides resistance to slip. The microstructure-sensitive crystal plasticity model employed here is based on the work of Shenoy and McDowell [7], with later updating and clarification of the

Table 1
Summary of equations used in the phase-field model.

Time-dependent Ginzburg–Landau evolution equation

$$\frac{\partial \eta_i(r,t)}{\partial t} = -L_i \frac{\partial F(t)}{\partial \eta_i(r,t)}, \quad i = 1,2,\ldots,Q \tag{1}$$

Total free energy of the microstructure

$$F(t) = \int \left\{ f_o(\eta_1(r,t),\eta_2(r,t),\ldots,\eta_Q(r,t)) + \frac{1}{2}\sum_{i=1}^{Q}\kappa_i[\nabla\eta_i(r,t)]^2 \right\} d^3r \tag{2}$$

Local free energy of ith grain

$$f_o = \sum_{i=1}^{Q}\left(-\frac{\alpha}{2}\eta_i^2(r,t) + \frac{\beta}{4}\eta_i^4(r,t)\right) + \gamma\sum_{k=1}^{Q}\sum_{j\neq i}^{Q}\eta_k^2(r,t)\eta_j^2(r,t) \tag{3}$$

Evolution of grain growth, specific form of Ginzburg–Landau equation

$$\frac{\partial \eta_i(r,t)}{\partial t} = -L_i\left(-\alpha\eta_i(r,t) + \beta\eta_i^3(r,t) + 2\gamma\eta_i(r,t)\sum_{j\neq i}^{Q}\eta_j^2(r,t) - \kappa_i\nabla^2\eta_i(r,t)\right), \quad i = 1,2,\ldots,Q \tag{4}$$

Incremental update of the order parameters

$$\eta_i(r,t+\Delta t) = \eta_i(r,t) + \frac{\partial \eta_i(r,t)}{\partial t}\Delta t, \quad i = 1,2,\ldots Q \tag{5}$$

equations and model parameters by Przybyla and McDowell [20], the latter being used in this work. The model is rate dependent and is calibrated to capture the mechanical response of IN100 at a simulation temperature of 650 °C (1200 °F). It incorporates the first-order effects of grain size, precipitate size and precipitate volume fraction, utilizing internal state variables to account for dislocation density and back-stress evolution. Table 2 summarizes the constitutive equations.

The kinematics of crystal plasticity are based on dislocation glide through the crystal lattice on slip planes and in slip directions. As evident in Eq. (6), the macroscopic deformation gradient, $\boldsymbol{F}$, is multiplicatively decomposed into a plastic part ($\boldsymbol{F}^P$) and an elastic part ($\boldsymbol{F}^e$). By invoking an isoclinic intermediate configuration shown in Fig. 2, the plastic deformation gradient can be defined to represent the collective glide of dislocations on each slip plane with the assumption that the crystal lattice is unaltered. Relative to the isoclinic configuration, the lattice is then assumed to undergo elastic distortion and rigid body rotation. The plastic velocity gradient in the intermediate configuration is calculated by summing the shearing rates $\dot{\gamma}^\alpha$ on the αth slip system, as given in Eq. (8). The terms s_0^α *and* m_0^α are unit vectors in the slip and slip plane normal directions, respectively.

The polycrystalline model employs a two-term flow rule [21], where D^α is the drag stress and κ^α is the threshold stress for the αth slip system (see Eq. (8)). The first term is intended to capture the dominant cyclic behavior with the threshold stress playing the role of yield strength. The second term describes thermally activated flow over a broader range of flow stress, including creep behavior below the initial yield strength. Additionally, for the slip system, the long-range Bauschinger effect is captured via the back-stress component. Short-range Bauschinger effects are associated with intergranular interaction, arising naturally from the polycrystalline FEM.

The hardening of the threshold stress, κ_λ^α, in Eq. (9) follows a Taylor relationship and is a function of the initial critical resolved shear stress, $\kappa_{o,\lambda}^\alpha$, a statistical coefficient accounting for the spatial arrangement of dislocations, β, the volume-averaged shear modulus, $\tilde{\mu}$, the volume-averaged Burgers vector, $\tilde{b}$, and the dislocation density, ρ_λ^α. Distinct initial critical resolved shear stresses are defined in Eqs. (12) and (13) for the 12 octahedral and 6 cube slip systems, respectively, where f'_{p1}, f'_{p2}, and f'_{p3} are normalized volume fractions of primary, secondary and tertiary precipitates. The terms c_{p1}, c_{p2}, c_{p3}, c_{gr} are calibration coefficients, and d_1, d_2, d_3, d_{gr} represent the average sizes of primary, secondary and tertiary precipitates along with the average grain size. Furthermore, Γ_{APB} is the anti-phase boundary energy, n_κ is an exponent in the range 1.0–1.2, and $\tau_{o,\gamma}^\alpha$ is the athermal lattice resistance of the solid solution γ-phase.

Non-Schmid effects [6,22–25] are accounted for in Eq. (16), where h_{pe}, h_{cb}, and h_{se} are constants. The terms τ_{pe}^α, τ_{cb}^α, and τ_{se}^α are the resolved shear stresses on the primary, cube and secondary slip systems. It should be noted that non-Schmid effects are only admitted on the octahedral slip systems. Eq. (17) prescribes evolution of dislocation density, where Z_o is the coefficient that moderates the scale effect associated with precipitation spacing

Table 2
Microstructure-sensitive crystal plasticity model.

Multiplicative decomposition of the deformation gradient

$$F = F^e \cdot F^p \tag{6}$$

Plastic velocity gradient

$$L_0^p = \dot{F}^p \cdot F^{p^{-1}} = \sum_{\alpha=1}^{N_{sys}} \dot{\gamma}^\alpha \left(s_0^\alpha \otimes m_0^\alpha\right) \tag{7}$$

Flow rule containing drag stress (D^α), backstress (χ^α) and threshold stress (κ^α)

$$\dot{\gamma}^\alpha = \left[\dot{\gamma}_1 \left\langle \frac{|\tau^\alpha - \chi^\alpha| - \kappa^\alpha}{D^\alpha} \right\rangle^{n_1} + \dot{\gamma}_2 \left\langle \frac{|\tau^\alpha - \chi^\alpha|}{D^\alpha} \right\rangle^{n_2}\right] \mathrm{sgn}(\tau^\alpha - \chi^\alpha) \tag{8}$$

Threshold stress with volume fraction averaged shear modulus/Burger's vector

$$\kappa_\lambda^\alpha = \kappa_{o,\lambda}^\alpha + \beta \tilde{\mu} \tilde{b} \sqrt{\rho_\lambda^\alpha} \tag{9}$$

$$\tilde{\mu} = (f_{p1} + f_{p2} + f_{p3})\mu_{\gamma'} + f_m \mu_m \tag{10}$$

$$\tilde{b} = (f_{p1} + f_{p2} + f_{p3}) b_{\gamma'} + f_m b_m \tag{11}$$

Octahedral and cube slip system initial critical resolved shear stresses

$$\kappa_{o,oct}^\alpha = \left[\left(\tau_{o,\gamma}^\alpha\right)^{n_\kappa} + \left(c_{p1}\sqrt{\zeta \frac{f'_{p1}}{d_1}} + c_{p2}\sqrt{\zeta \frac{f'_{p2}}{d_2}} + c_{p3}\sqrt{\zeta f'_{p3} d_3} + \frac{c_{gr}}{\sqrt{d_{gr}}}\right)^{n_\kappa}\right]^{1/n_\kappa} + \left(f'_{p1} + f'_{p2}\right)\tau_{ns}^\alpha \tag{12}$$

$$\kappa_{o,cub}^\alpha = \left[\left(\tau_{o,\gamma}^\alpha\right)^{n_\kappa} + \left(c_{p1}\sqrt{\zeta \frac{f'_{p1}}{d_1}} + c_{p2}\sqrt{\zeta \frac{f'_{p2}}{d_2}} + c_{p3}\sqrt{\zeta f'_{p3} d_3} + \frac{c_{gr}}{\sqrt{d_{gr}}}\right)^{n_\kappa}\right]^{1/n_\kappa} \tag{13}$$

Anti-phase boundary energy, normalized precipitate volume fractions and non-Schmid terms

$$\zeta = \frac{\Gamma_{APB}}{\Gamma_{APB\_ref}} \tag{14}$$

$$f'_{p1} = \frac{f_{p1}}{f_{p1} + f_m}, \quad f'_{p2} = \frac{f_{p2}}{f_{p2} + f_m}, \quad f'_{p3} = \frac{f_{p3}}{f_{p3} + f_m} \tag{15}$$

$$\tau_{ns}^\alpha = h_{pe}\tau_{pe}^\alpha + h_{cb}\left|\tau_{cb}^\alpha\right| + h_{se}\tau_{se}^\alpha \tag{16}$$

Evolving dislocation density equation (internal state variable)

$$\dot{\rho}_\lambda^\alpha = h_0\left\{Z_o + k_1\sqrt{\rho_\lambda^\alpha} - k_2\rho_\lambda^\alpha\right\}|\dot{\gamma}^\alpha| \tag{17}$$

Precipitate scaling and effective spacing terms

$$Z_o = \frac{k_\delta}{\tilde{b} d_{\delta eff}} \tag{18}$$

$$d_{\delta eff} \approx \left(\frac{2}{d_{2\delta}}\right)^{-1} \tag{19}$$

Backstress term (internal state variable)

$$\dot{\chi}_\lambda^{(\alpha)} = C_\chi\left\{\eta\tilde{\mu}\tilde{b}\sqrt{\rho_\lambda^\alpha}\,\mathrm{sgn}(\tau^\alpha - \chi_\lambda^\alpha) - \chi_\lambda^\alpha\right\}|\dot{\gamma}^\alpha| \tag{20}$$

Ratio of geometrically necessary total dislocation density

$$\eta = \frac{\eta_o Z_o}{Z_o + k_1\sqrt{\rho_\lambda^\alpha}} \tag{21}$$

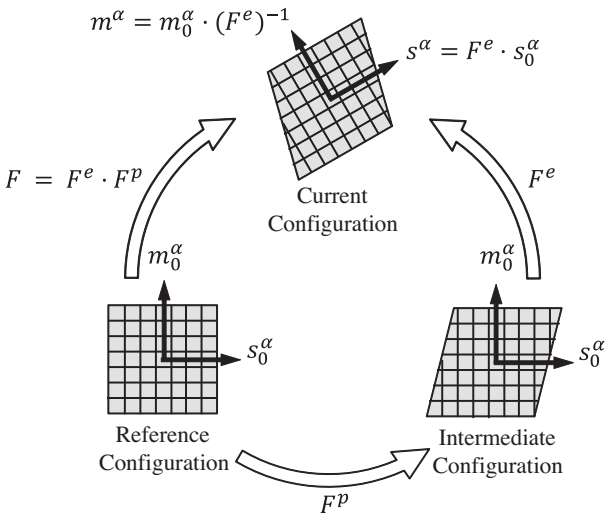

Fig. 2. Elastoplastic decomposition of the deformation gradient tensor.

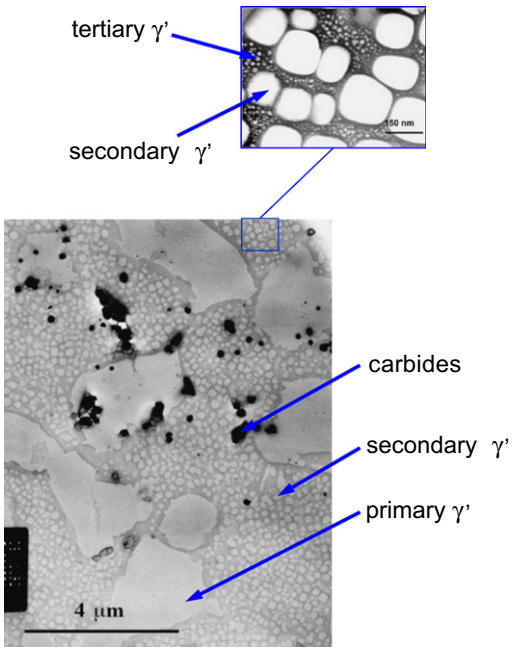

Fig. 3. TEM micrographs of IN100 microstructure from Ref. [30].

attributed to the production of geometrically necessary dislocations. An effective value of precipitate spacing is defined by Eq. (18). Additionally, Eq. (17) captures the hardening and dynamic recovery of the material based on the Kocks–Mecking model [26,27]. The back-stress in Eq. (20) evolves in rough accordance with the ratio of geometrically necessary to total dislocation densities (Eq. (21)). As previously mentioned, the back-stress term captures the Bauschinger effect associated with the heterogeneous pile-up of dislocations at precipitate–matrix interfaces, as well as slip reversibility under low-cycle fatigue loading. Complete details about the development and calibration of the polycrystalline IN100 microstructure-sensitive model can be found in Ref. [7]. The model was implemented as a user-defined material subroutine (UMAT) within the ABAQUS [28] finite-element platform. Simulation results are presented in Section 4.

3. IN100 microstructure

Alloys such as IN100 are produced by a powder metallurgy process, followed by isothermal forging and a multi-step heat treatment. The material is categorized according to the particular heat treatment applied to the alloy, either subsolvus or supersolvus. A subsolvus material is processed at a temperature below the solutionizing temperature, whereas a supersolvus material is processed at a temperature above the solutionizing temperature. Both materials undergo further aging steps to optimize their γ' precipitate size distributions and volume fractions in order to enhance the mechanical performance of the material.

The IN100 material considered here consists of a fine-grained subsolvus microstructure that was extensively characterized by Wusatowska-Sarnek et al. [29,30]. The microstructure consists of a trimodal distribution of primary γ' (~1.71 μm diameter), secondary γ' (~120.2 nm) and tertiary γ' (~8.5 nm) precipitates. The average grain size of the material is ~3.5 μm. Volume fractions of the primary γ', secondary γ' and tertiary γ' are 0.199, 0.305 and 0.051, respectively. Two transmission electron microscopy (TEM) images from Ref. [30] are shown in Fig. 3. The bottom image is a bright-field micrograph consisting of primary and secondary γ' precipitates. The top image is a higher-resolution dark-field micrograph that captures the distribution of tertiary and secondary precipitates within the structure. The material also contains carbide precipitates and twin boundaries (not shown in Fig. 3).

A 3-D digital representation of the initial IN100 microstructure was created via an automated serial sectioning EBSD scheme implemented by Groeber et al. [31]. It consists of 184 serial sections reconstructed into a volume of 96 μm × 36 μm × 47 μm with a spatial resolution of 250 nm in the x-, y- and z-directions. Additionally, the crystallographic texture for each of the approximately 10.5 million voxels was tabulated from the EBSD process

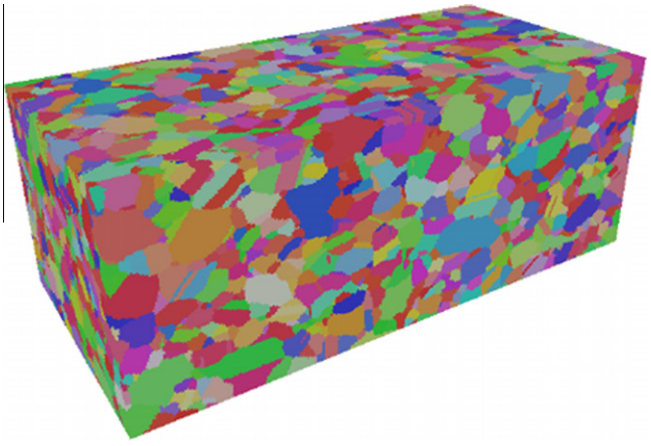

Fig. 4. Reconstructed 96 × 46 × 36 μm^3 IN100 microstructure [31].

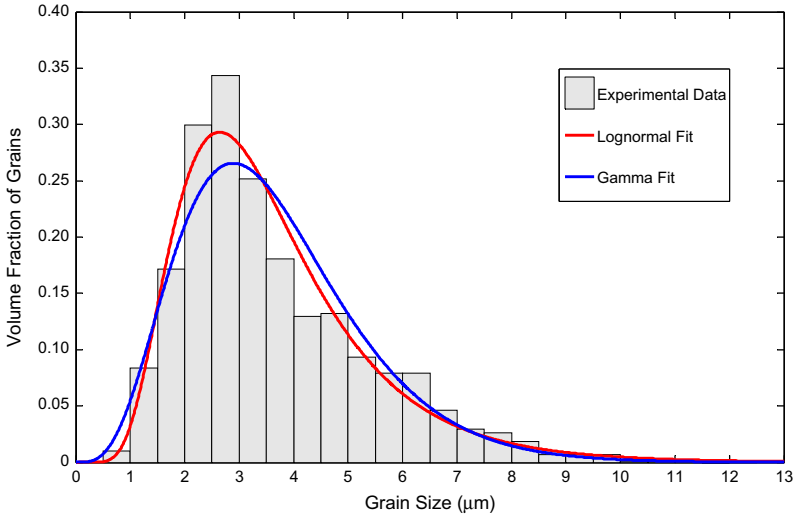

Fig. 5. IN100 grain size distribution plots with measured histogram shaded in gray, log-normal distribution fit (red curve) and gamma distribution fit (blue curve).

with grain identification and assignment based on a of 5° angle of misorientation. The process resulted in the 4373 grains plotted in Fig. 4. Carbides were not captured in the process and twin boundaries were removed from the reconstructed dataset, resulting in 3165 net grains (1818 non-edge grains). A detailed description of the characterization and reconstruction procedures can be found in Ref. [31].

The line intercept method described in ASTM E112 [32] is commonly used to measure grain size distributions. This stereographic method involves the counting of grain boundary intersections with a grid of lines that are overlaid onto a 2-D micrograph. Another approach used in orientation imaging microscopy (OIM) is to calculate the equivalent circle diameter [33]. In this method, the area (A) of each grain within the 2-D plane is tabulated. Then, by

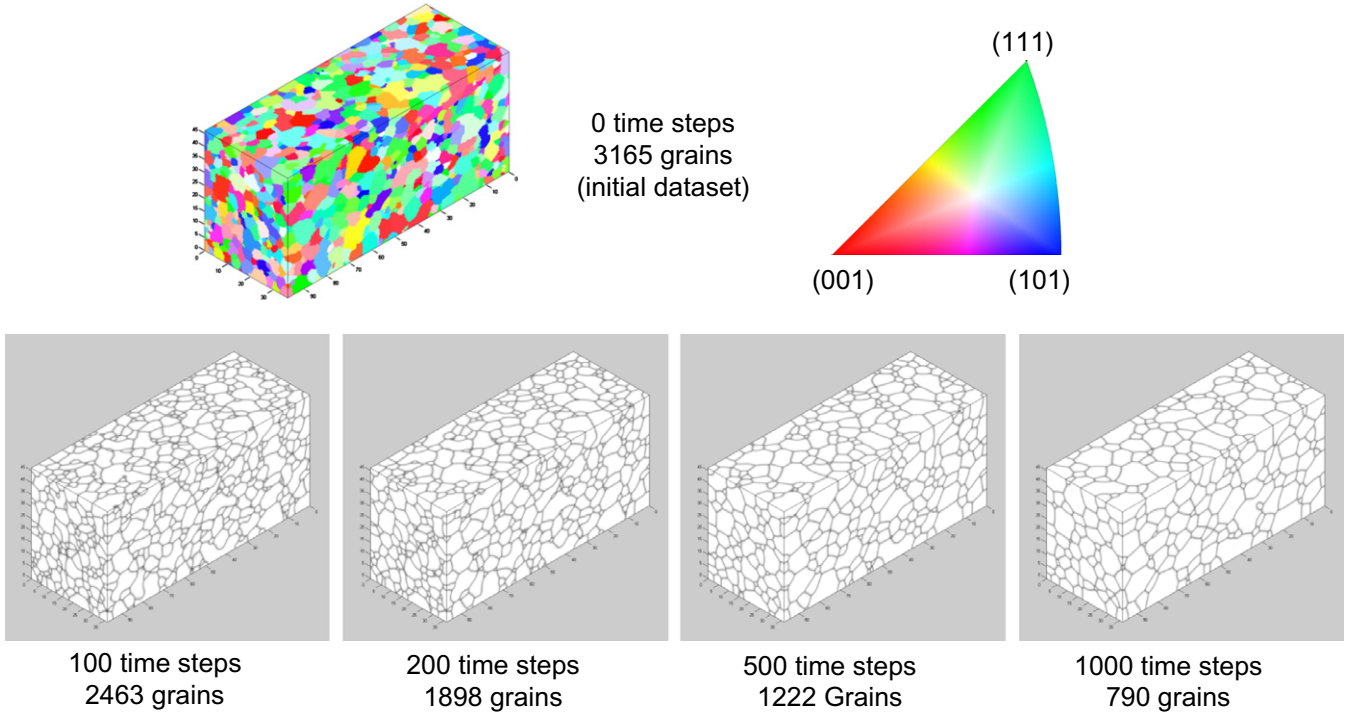

Fig. 6. Output from the grain growth simulations at time increments of 0, 100, 200, 500 and 1000. The number of grains reduced from 3165 to 790 over 1000 time steps.

Table 3
Summary of grain size statistics for the IN100 grain growth simulation.

Time steps	Number of grains	Non-edge grains	Average grain volume (μm^3)	Average equivalent sphere diam. (μm)	Lognormal fit (μm)	Lognormal error (average/st.dev.)	Gamma fit (μm)	Gamma error (average/st.dev.)
0	3165	1818	45.27 ± 75.08	3.64 ± 1.73	3.64 ± 3.17	0.1%/83.4%	3.64 ± 2.72	0.0%/57.4%
100	2463	1427	54.61 ± 91.81	3.70 ± 2.06	3.81 ± 7.33	2.9%/256.6%	3.70 ± 4.58	0.0%/122.8%
200	1898	1017	72.95 ± 110.98	4.20 ± 2.16	4.32 ± 8.24	2.7%/281.2%	4.20 ± 5.26	0.0%/143.5%
500	1222	590	110.79 ± 154.11	5.03 ± 2.26	5.14 ± 8.55	2.2%/277.6%	5.03 ± 5.78	0.0%/155.2%
1000	790	347	157.77 ± 204.45	5.68 ± 2.55	5.80 ± 10.94	2.1%/329.4%	5.68 ± 7.46	0.0%/192.9%

assuming a circular grain shape, the equivalent grain diameter is given by:

$$D_{2D} = 2\sqrt{\frac{A}{\pi}} \tag{22}$$

Although these methods produce consistent results for a range of materials, the calculated grain size values do not correlate well with results obtained from 3-D datasets [32,34]. As a result, the grain diameters estimated from the 2-D datasets are generally undersized, requiring a correction factor to equate them to 3-D grain statistics. All digital microstructures used in this study contain voxellated structures. Based on a voxel size of 0.25 μm × 0.25 μm × 0.25 μm, the volume of each voxel is 0.015625 μm^3. By multiplying the number of voxels in each grain by the voxel volume (V), a distribution of grain

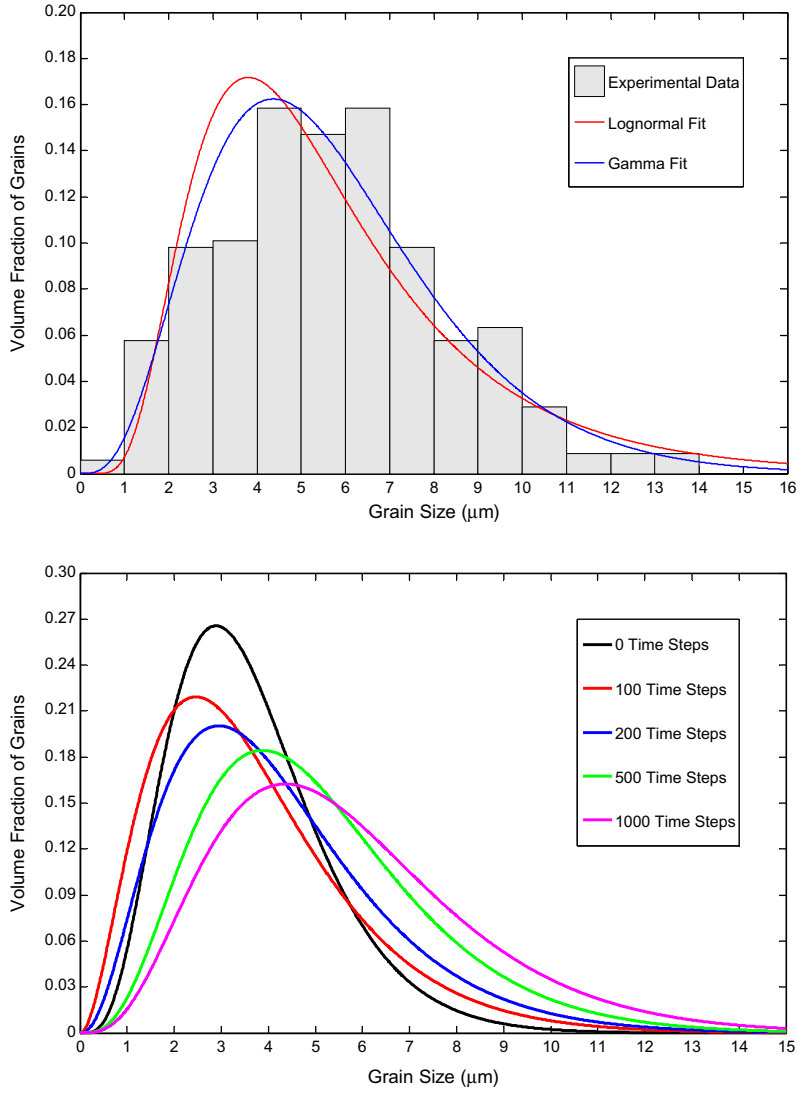

Fig. 7. (top) Grain size distribution for dataset at 1000 time steps; (bottom) comparison of grain size distribution for 0, 100, 200, 500 and 1000 time steps based on the gamma curve fit.

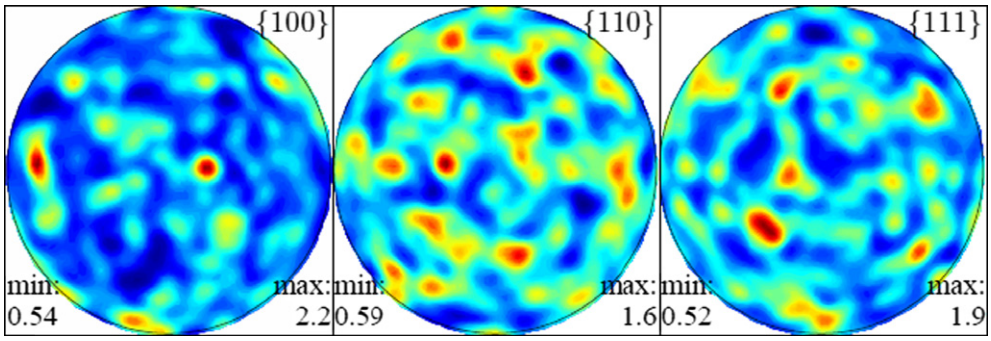

Fig. 8. Pole figure plots of initial microstructure illustrating the uniform random texture of the IN100 material.

volumes can be tabulated. The grain volumes are converted to equivalent sphere diameters for each grain in the dataset according to:

$$D_{3D} = \sqrt[3]{\frac{6V}{\pi}} \tag{23}$$

Fig. 5 presents plots of the grain size distribution of the initial microstructure based on Eq. 23 for the reconstructed subsolvus IN100 material using MATLAB [35], consisting of three separate distributions overlaid onto a single plot. The histogram, highlighted in gray, was binned according to Scott's rule [36]. The average grain size was determined to be 3.64 μm with a standard deviation of ±1.73 μm. The red[1] and blue distributions in Fig. 5 represent fits to the grain size distribution based on the log-normal and gamma functions, respectively.

4. Results

4.1. PFM simulations for grain growth

To simulate grain growth in the IN100 material, the PFM must be properly calibrated. Spatial calibration was performed by first inputting the 3-D reconstructed dataset from Groeber [31] into the PFM. The process was simplified due to the fact that both the PFM and IN100 datasets share a voxel-based structure. Each voxel from the reconstructed microstructure with its associated x,y,z-coordinates is directly assigned to the uniform Cartesian coordinate system representing the phase-field mesh. Next, each grain region in the dataset is assigned a unique order parameter value based on the grain assignment and corresponding orientation in the first step. Hence, the 3165 order parameters directly correlate to the 3165 grains found in the reconstructed microstructure. The final step consists of assigning an η value of 1 to each voxel in the dataset, thereby completing the spatial calibration.

Once the PFM was calibrated, it was incremented through 1000 time steps to simulate grain growth of the IN100 material. Time step calibration was not undertaken in this work, and hence the simulation time does not correspond to physical time; however, 1000 time steps are sufficient to evolve grain growth to the desired final level. Results from the analysis were recorded at 100, 200, 500 and 1000 time steps and are shown in Fig. 6 along with the initial dataset at $t = 0$. Through the course of the simulation, the number of grains was successively reduced from 3165 to 2463, 1898, 1222 and 790 grains, respectively, at the specified number of time steps.

Grain size statistics were calculated at increments of 0, 100, 200, 500 and 1000 time steps. The full $97 \times 36 \times 47$ μm^3 volume was sampled and only interior grains were included to ensure statistical reliability (no effects of periodic surfaces). Grain volume and equivalent sphere diameter calculations were determined from Eq. (23). The statistics are summarized in Table 3, indicating that the average grain size increased from 3.64 μm for the starting dataset to 5.68 μm for the final dataset.

Fig. 7 (top) shows a histogram of the grain size distribution for the 1000 increment dataset. Similar to Fig. 5 in Section 4.1, two additional functions are plotted, the red curve representing a log-normal distribution fit and the blue curve a gamma distribution fit to the experimental data. Traditionally, the log-normal distribution has been used to statistically represent grain size measurements. Vaz and Fortez [37] suggested that the gamma distribution better captures the grain size distribution for recrystallized microstructures. Kong et al. [34] concluded that the gamma distribution better fits the size distribution of a set of spherical particles in a two-phase composite. Moreover, Wang et al. [38] reported that the gamma distribution offered a better statistical fit to a set of 3-D microstructures obtained through Monte Carlo and PFM. In the case of the 3-D phase-field data presented here, the gamma function offers an improved statistical fit to the measured data. The values of equivalent sphere diameter for each of the five datasets are listed in Table 3. For each of the datasets, the gamma distribution exactly matched the average grain size, whereas the log-normal distribution deviated by up to 2%. In addition, the standard deviation values for the gamma distribution were much closer to the experimental data than those of the log-normal fit distribution.

As expected for the grain growth simulation, the results in Table 3 demonstrate a reduction in the number of grains

[1] For interpretation of color in Figs. 1, 3–13, A1 and A2, the reader is referred to the web version of this article.

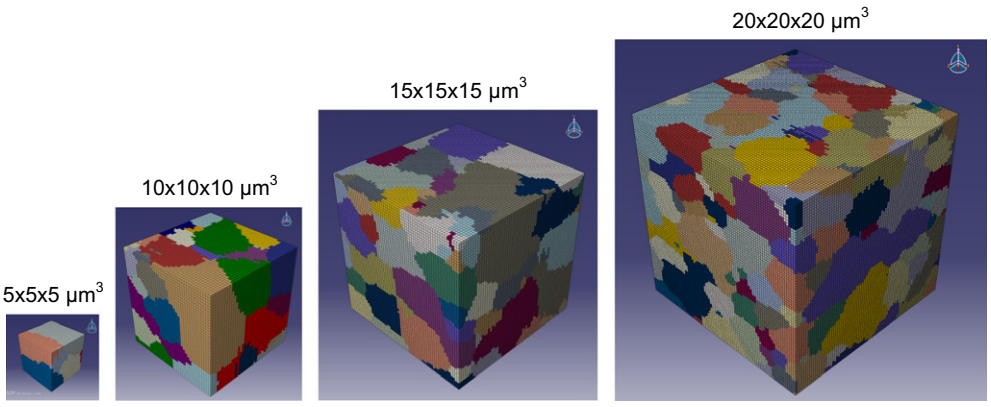

Fig. 9. Size comparison of FEM input files for selected SVEs (initial microstructure shown).

Table 4
Comparison of FEM input files.

Dataset size (μm^3)	Mesh size	Number of elements	Degrees of freedom	Number of grains in SVE		
				0 Steps	500 Steps	1000 Steps
$5 \times 5 \times 5$	$21 \times 21 \times 21$	10,649	31,947	9	5	4
$10 \times 10 \times 10$	$41 \times 41 \times 41$	68,921	222,267	45	22	13
$15 \times 15 \times 15$	$61 \times 61 \times 61$	226,981	714,987	108	45	30
$20 \times 20 \times 20$	$81 \times 81 \times 81$	531,441	1654,107	246	108	69
$35 \times 35 \times 35$	$141 \times 141 \times 141$	2863,289	8589,867	910	386	246

as the analysis proceeds, with a simultaneous increase in average grain size and standard deviation. Fig. 7 (bottom) offers a visual confirmation of this change in grain size distribution for the 0, 100, 200, 500 and 1000 time step datasets. For each incremental dataset, the height of the distribution declines due to a decrease in volume fraction of grains, while the width of the distribution increases due to a larger variation of grain sizes within the statistics. It is interesting that the probability of occurrence of large grains of size 10–15 μm increases by more than an order of magnitude during coarsening. This has important implications for minimum fatigue life, for example, as demonstrated in the work of Przybyla and McDowell on IN100 [20].

Pole figures in Fig. 8 represent the initial crystallographic texture of the IN100 datasets as calculated with MTEX [39]. The plot shows that the IN100 material has a uniform random texture with peak intensities of 2.2×, 1.6× and 1.9× random in the {100}, {110} and {111} directions, respectively. Pole figures for the datasets recorded at 100, 200, 500 and 1000 time steps are not shown here due to negligible changes in texture. A small increase in peak intensity to 3.5×, 2.2× and 2.7× random were recorded for the {100}, {110} and {111} directions, respectively, for the dataset annealed to 1000 time steps. Such results are, of course, significantly affected by the assumption of isotropic grain boundary mobility and energy in the present work. In reality, the grain boundary distribution exhibits a substantial range of energy and mobility.

4.2. Finite-element modeling

A methodology was developed to link voxellated 3-D datasets, whether experimentally obtained (EBSD) or synthetically generated (PFM), to the microstructure-sensitive finite-element model introduced in Section 2.2. Because voxellated structures can be readily converted to hexahedral meshes, reduced integration C3D8R [28] elements with random periodic boundary conditions [40–43] were utilized for the finite-element simulations. As illustrated in Fig. 1, this linkage between the phase-field and finite-element models has two-way character. Changes in material parameters resulting from the finite-element simulation, such as texture evolution with imposed deformation and dislocation density increase, can in principle be conveyed back to the phase-field model. This can assist modeling of strain-induced recrystallization, for example. However, this is not undertaken in the current work which focuses on one-way use of PFM to provide input to FEM simulation of stress–strain behavior of successively coarsened grain structures, neglecting coarsening of the finer-scale precipitate structures and the influence of cold work on the driving force for coarsening.

The complete IN100 dataset contains approximately 10.5 million voxels and is too large to use in finite-element simulations. Therefore, a set of smaller subvolumes, so-called statistical volume elements (SVEs), were employed to construct a statistical ensemble of stress–strain simulations, as shown in Fig. 9. The SVEs ranged in size from $5 \times 5 \times 5\ \mu m^3$ to $35 \times 35 \times 35\ \mu m^3$, corresponding to a

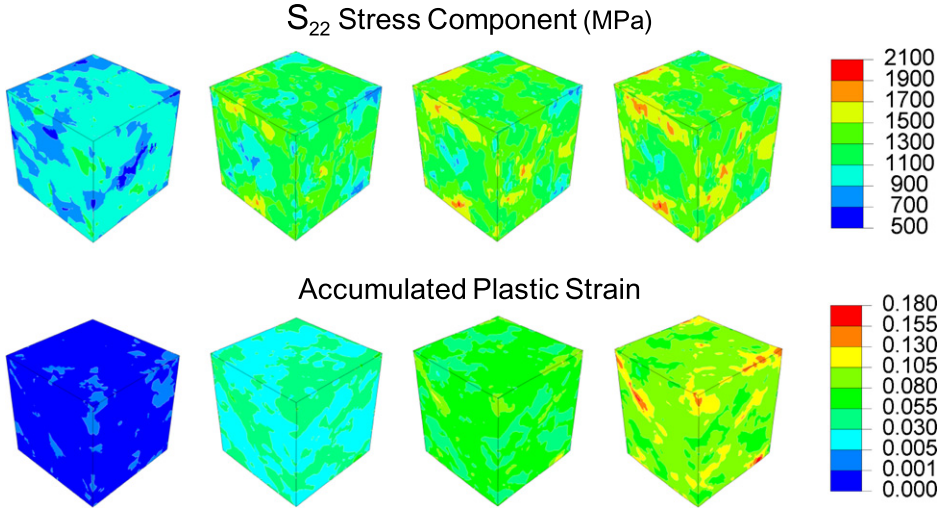

Fig. 10. 3-D contour plots representing the S_{22} stress component (top) and accumulated plastic strain (bottom) for the $15 \times 15 \times 15\ \mu m^3$ SVE at increments (from left to right) of 0.5%, 3.5%, 6.5% and 9.5% true strain, respectively.

mesh size (i.e. number of elements along each edge of the SVE) ranging between $21 \times 21 \times 21$ and $141 \times 141 \times 141$. The number of elements in each SVE varied from 10,649 to 2863,289. Meshes were created for three of the five phase-field datasets, namely the outputs at 0, 500 and 1000 time increments. A complete listing of mesh characteristics, including the number of grains contained in each SVE, appears in Table 4.

A comprehensive listing of input variables for the microstructure-sensitive crystal plasticity model can be found in Ref. [20]. Parameter values of $\beta = 0$ and $C_\chi = 10.96$ MPa were used in lieu of the values reported in Ref. [20] because they depend on precipitate distributions that differ from those used in the previous study. All other parameters remained constant for each of the FEM simulations except for average grain size. Mean grain size values of 3.64 μm (ASTM 13.2), 5.03 μm (ASTM 12.3) and 5.68 μm (ASTM 12.0) were used for the datasets recorded at 0, 500 and 1000 time steps, respectively. Crystallographic texture data, defined by a set of three Euler angles, were obtained experimentally from EBSD measurements but are not tabulated due to space limitations. The values of precipitate volume fraction and mean size for each population of precipitates reported in Section 3 were held constant between datasets even though realistic grain growth experiments would result in variation of these parameters. This limitation could be addressed by the development of a more complex two-phase grain growth model that explicitly addresses both grain growth and precipitate coarsening.

The large numbers of elements in the IN100 meshes necessitates a substantial amount of memory for solutions. Additionally, the computationally intense nature of the finite-element simulations results in lengthy run times. To offset these limitations, the IN100 ABAQUS UMAT [28], written as a FORTRAN subroutine, was modified and

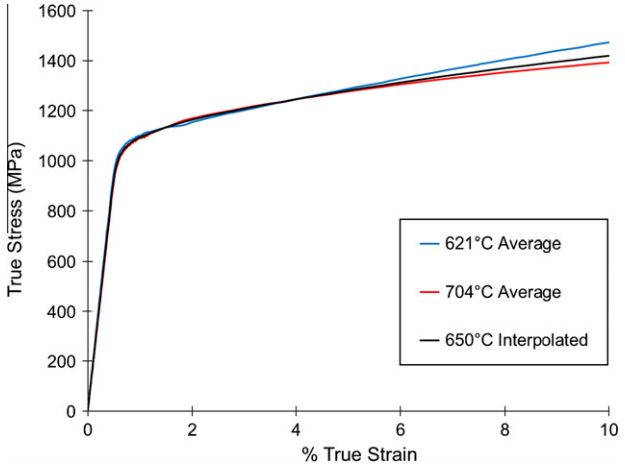

Fig. 11. Averaged experimentally obtained true stress–strain curves at 621 °C (blue curve) and 704 °C (red curve). The black curve represents the interpolation stress–strain curve at 650 °C. A strain rate of $8.33 \times 10^{-5}\ s^{-1}$ was used for all experiments.

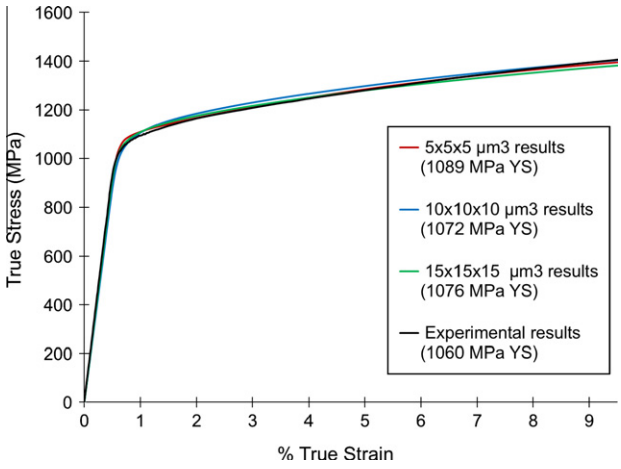

Fig. 12. Comparison of IN100 experimental true stress–strain results to simulations and the impact of SVE size on the solution.

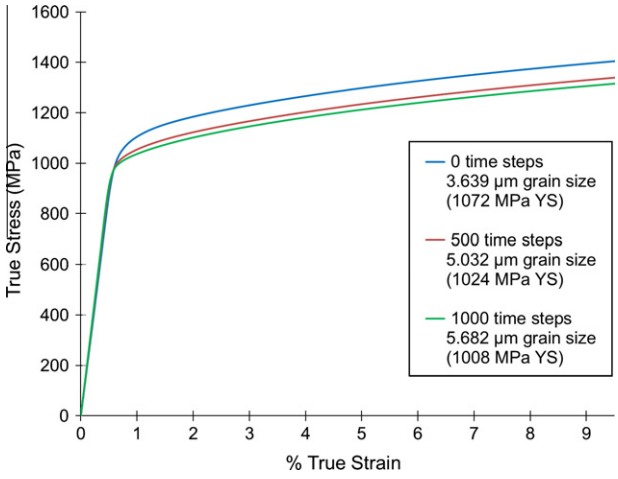

Fig. 13. Simulated stress–strain response for 0, 500 and 1000 time step datasets, representing grain size effects for coarsened microstructures.

ported to run within a high-performance computing environment. Both MPI-based and thread-based parallelizations were utilized. The NSF TeraGrid high-performance computing network was employed for all finite-element computations. Utilizing 64 cores, a speed-up value near 28 was achieved by utilizing sufficient compute nodes to ensure the simulation ran within system memory and avoided unnecessary internodal communication. The results indicate that simulation time scales as the square root of the degrees of freedom within the system. The interested reader can find a more detailed discussion of benchmark results in the Appendix.

4.3. FEM results

Fig. 10 presents 3-D stress–strain plots from simulations for uniaxial tension of subsolvus IN100 at 650 °C (1200 °F). The contour plots illustrate the evolution of stress and strain in the microstructure as the simulation progresses. The top row of plots represents the S_{22} Cauchy stress component and the bottom row represents the von Mises accumulated plastic strain within the applied strain window of 0.5–9.5%. Similar plots can be employed not only to visualize mechanical response but to find localized regions within the microstructure with high levels of stress or strain. For example, regions with elevated values of accumulated plastic strain can be analyzed using fatigue indicator parameters [20,44,45] to quantify microstructure sensitivity of the driving force to form and grow small fatigue cracks [20].

Experimental stress–strain curves from Milligan [46] are considered in this work. The data consist of three stress–strain curves at 621 °C (1150 °F) and five curves at 704 °C (1300 °F) recorded at a strain rate of $8.33 \times 10^{-5}\,s^{-1}$, relevant to the response of the initial microstructure of the present study. After averaging the three stress–strain plots at 621 °C separately from the five stress–strain curves at 704 °C, an interpolated stress–strain curve at 650 °C was calculated from the two averaged curves, as shown in Fig. 11. At true strain values less than 5%, there is little difference between the experimental stress–strain curves recorded at 621 and 704 °C. Above 5% true strain, the true stress values for the 704 °C curve begin to diverge lower than for the 621 °C curve. Although the temperature dependence of flow stress is not linear due to thermal activation, the interpolated 650 °C curve is considered reasonable owing to the weak temperature dependence of the initial yield strength within this window of temperature, as illustrated by the black curve in Fig. 11. Based on the 0.2% offset criterion, the interpolated curve has a yield strength value of 1060 MPa.

Fig. 12 contains true stress–strain responses for the initial microstructure from the microstructure-sensitive finite-element simulation, with the red, blue and green curves corresponding to the $5 \times 5 \times 5\ \mu m^3$, $10 \times 10 \times 10\ \mu m^3$ and $15 \times 15 \times 15\ \mu m^3$ SVEs, respectively. The black curve represents the interpolated experimentally based stress–strain curve from Fig. 11. Values of yield strength were 1089, 1072 and 1076 MPa for the three datasets, respectively.

In general, as the SVE size increases, the predicted values of mechanical response should converge to the experimental values corresponding to a statistically representative volume. Unfortunately, SVE sizes larger than $15 \times 15 \times 15\ \mu m^3$ were too large to simulate due to practical limitations of available memory and runtime. A parametric study would be necessary to define a minimum SVE size and the number of SVEs required to constitute a representative volume element (RVE), but this is beyond the scope of the present work.

Finally, the simulated effect of grain size on the mechanical response of IN100 is plotted in Fig. 13. Based on an SVE size of $10 \times 10 \times 10\ \mu m^3$, FEM results are plotted for each of the PFM datasets at 0, 500 and 1000 time steps. It is not surprising that the flow stress decreases as grain size increases since the grain size terms in Eqs. (12) and (13) follow a Hall–Petch relationship. The dataset for the initial microstructure (0 time step) had the highest yield strength value of 1072 MPa, followed by values of 1024 and 1008 MPa for the 500 and 1000 increment datasets, respectively.

5. Discussion

As part of this research, a phase-field model was linked to a microstructure-sensitive finite-element model. A realistic IN100 microstructure characterized using EBSD on serial sections by Groeber et al. [31] was used to calibrate the phase-field model. A single-phase grain growth simulation was executed through 1000 time steps, resulting in a reduction in number of grains during coarsening from 3165 to 790. FEM simulations conducted within a high-performance computing environment scaled well to 64 cores and achieved maximum speed-up rates of nearly 28. Simulation results for 650 °C showed good agreement with experimentally obtained stress–strain data for the initial

microstructure. A discussion of the limitations, approximations and suggestions for future research related to the phase-field model, material characterization, and finite-element model follows below.

The phase-field model utilized in this study was based on a binary Ni–Al system. Augmentation of the model to allow for additional alloy elements in the thermodynamic calculations would improve applicability of the grain growth results. Additionally, the current PFM does not consider the effect of depleted zones on precipitate formation/growth or account for inclusion of hard phases within the matrix or along grain boundaries that are known to affect fatigue life and grain boundary mobility within Ni-base superalloys. Recently, Chang et al. [15] utilized PFM to study the ability of second-phase particles to inhibit grain boundary migration. Although the model used in this research was calibrated spatially from an experimentally characterized microstructure, the issue of time calibration to better correlate the model to known process path histories needs to be addressed. Lastly, development of a two-phase grain growth model ($\gamma-\gamma'$) to enable the simultaneous coarsening of both γ' precipitates and grains is warranted.

Experimental characterization of the IN100 microstructure is critical to the calibration of both the phase-field and finite-element models, serving as the basis for the realistic grain structures presented here. A limitation of the existing IN100 dataset is the absence of twin boundaries within the reconstructed microstructure. Because the subsolvus IN100 twins were similar in width to the scan resolution, they could not be properly recovered and were thus removed from the dataset [31]. However, twin boundaries are known to affect the mechanical properties of metals as they effectively reduce the grain size of the structure and provide barriers for dislocation migration, thus influencing the fatigue response of the material. Utilizing higher-resolution EBSD scans would allow for more accurate recovery and reconstruction of the twin boundaries.

The FEM approach does not fully address the role of grain boundary structure on dislocation slip transfer between grains. Rohrer et al. [47,48] have devoted significant efforts to reconstructing grain boundary networks from 3-D EBSD datasets and calculating the associated distribution of grain boundary character and grain boundary energy within the microstructure, which can provide valuable input into PFM simulations and enhanced FEM simulations that employ constitutive equations for slip transfer at grain boundaries.

Wilkinson and colleagues [49] have described a method to accurately determine the full elastic strain tensor from EBSD scan data. This elastic strain tensor is beneficial for both calibrating and verifying finite element models. Adams et al. [50,51] augmented the technique by generating synthetic strain-free electron backscatter patterns for purposes of cross-correlation and estimated values of lattice curvature and dislocation density in addition to elastic strain. Generating 3-D maps of dislocation density for a given EBSD dataset would improve the accuracy of FEM results since the simulation could be calibrated to experiments with regard to dislocation density evolution.

Microstructure-sensitive FEM requires continued research in several areas. Recently, McDowell [52] discussed key challenges for future progress, including: modeling over multiple length scales, statistical behavior of dislocations and formation of subgrains, multiscale kinematics, treatment of grain boundaries, and a discussion of top-down vs. bottom-up modeling schemes. He further elaborated on the need to advance discrete dislocation and crystal plasticity theory within the context of concurrent and hierarchical multiscale modeling strategies [53]. Several areas that may impact future FEM development are as follows:

(i) The concept of minimum SVE size and number of SVEs required to simulate an RVE requires further development. As argued by Fullwood et al. [54], the ergodic assumption must be invoked when using an ensemble of SVEs to fit an RVE. This requires that the statistical average of the desired property within the SVEs must be equivalent to the statistics for the RVE. The goal in selecting an SVE size is to minimize the average error and standard deviation between the chosen set of SVEs and the RVE, and simultaneously to minimize SVE size. Unfortunately, these two factors are in direct competition since the SVE size must be increased in order to reduce error. Utilizing two-point statistics, Niezgoda and coworkers [55] illustrated a procedure to determine the appropriate SVE size for both a two-phase composite and a polycrystalline metal. McDowell et al. [56] have elaborated on the use of a statistically equivalent RVE (SERVE) for general problems without phase rearrangement/damage and RVE sets for more complex problems that include evolution of damage within the microstructure.

(ii) Recent work by Przybyla and McDowell [20] concluded that as few as 25 SVEs were sufficient to fit an extreme value distribution of the Fatemi–Socie fatigue indicator parameter at 97% confidence utilizing a $28 \times 28 \times 28$ element mesh containing 77 grains. Further, they concluded that the primary zone of influence on any given grain extended to the two nearest neighbors of the grain, assuming periodic boundary conditions are imposed in the simulation. Additionally, it was observed that the extreme value fatigue indicator parameter did not vary substantially for edges with 12 or more elements along the edge. Based on these conclusions, an SVE volume size containing 20–30 elements and 5 grains per edge should be sufficient to conduct a parametric study for the research presented here. From Table 4, this corresponds to an intermediate SVE size between $10 \times 10 \times 10\ \mu m^3$ and $15 \times 15 \times 15\ \mu m^3$ to ensure a sufficient number of grains, but a SVE size between

$5 \times 5 \times 5\ \mu m^3$ and $10 \times 10 \times 10\ \mu m^3$ to satisfy mesh density requirements. As a result, additional work to coarsen the mesh density is needed in addition to the parametric study to define minimum SVE size and number of SVEs required to constitute an RVE response.

(iii) The existing finite-element model employs voxellated meshes to represent grain boundaries. In contrast to real microstructures, voxellated grain edges are jagged by nature. Future work to compare smooth boundary meshes to the voxellated meshes might be warranted if advances are made in constitutive models for grain boundary slip transfer. Both phase-field and finite-element models would perhaps benefit from multiscale approaches that permit explicit consideration of the precipitates, depending on the goals and purpose of the simulations.

(iv) Methods to reduce computation time are of great practical relevance. In addition to the parallel computing approach adopted in this work, another approach to reduce simulation time is to reduce the mesh density of the simulation volume. Lewis and Geltmacher [57] pursued this route by coarsening a voxellated mesh by sampling every fourth pixel in the x–y plane of the dataset but retaining each of the sections in the z-direction. The result was significantly reduced computation time with some loss in grain boundary fidelity. A more advanced technique would be to apply a similar procedure within the 3-D grain structure by coarsening the mesh at the interior of the grains but preserving a more refined structured mesh near grain boundary interfaces. Lastly, statistical continuum mechanics can be developed to replace traditional FEM methodologies. For example, Garmestani et al. [58] utilized two-point statistics to simulate the mechanical response and texture evolution of an fcc polycrystal subjected to large plastic deformation. Conditions of compatibility and stress equilibrium within the model were satisfied by numerically computing a Green's function solution for the set of partial differential equations. More recently, Ahmadi et al. [59] described a double continuity model that accurately modeled the evolution of pair correlation statistics under large plastic strain; in this work, an Eulerian-based model that employed a finite-difference method was developed to satisfy conservation of both mass and orientation. Finally, Kalidindi and coworkers [60–62] have formulated a type of statistical continuum approach termed "Materials Knowledge System" (MKS) to facilitate the bidirectional flow of process–structure–property correlations over multiple length scales. The technique utilizes influence functions calibrated from FEM simulations to link the localized material response to the macroscopic response over a wide range of applied conditions. The main advantage of these statistical correlation-based approaches over traditional FEM methods is a significant reduction in computation time with certain simplifying assumptions.

6. Conclusions

The objective of this work has been to introduce a methodology whereby phase-field and finite-element models can be one-way coupled (from phase field to finite element) to enable predictive process–structure–property relations. A 3-D digital microstructure recovered through OIM provided a realistic grain structure necessary for calibration of the models. Experimental procedures for determining grain size distribution were described and a comparison made between the log-normal and gamma distributions. The methodology was demonstrated for a subsolvus IN100 Ni-based superalloy. Results for both grain growth and microstructure-sensitive finite-element simulations were presented and ideas for future research were detailed. The following conclusions and observations can be drawn from the study:

- The present work required only a one-way coupling to predict the mechanical response of IN100. However, in order to establish top-down material design methods, future work will need to establish a fully two-way linkage.
- Based on the research results, EBSD is a useful characterization technique to not only assist in reconstruction of realistic 3-D microstructures but to also spatially calibrate the phase-field and finite-element models. It is noted that sequences of time-resolved EBSD datasets recovered over a range of temperatures are necessary to fully calibrate phase-field predictions of evolving microstructure.
- For the PFM simulations for grain growth in IN100, the gamma distribution was found to better represent the grain size distribution than the traditional log-normal distribution.
- The simulation time of the finite-element model scales as the square root of the number of degrees of freedom for both single and multicore computing environments.

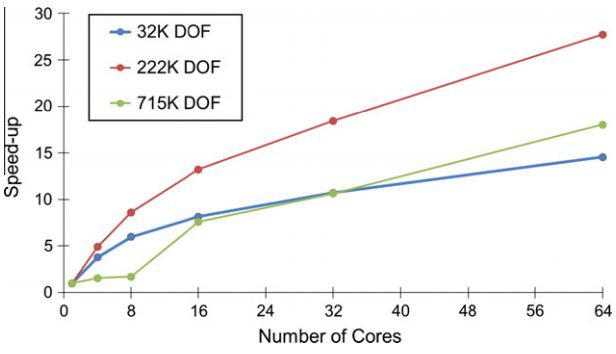

Fig. A1. ABAQUS speed-up vs. number of cores.

Table A1
Impact of model size on simulation time.

Dataset size (μm^3)	Number of elements	Degrees of freedom	Iterations (6% strain)	Number of cores	Variables per core	Memory per node (GB)	Iteration time (min)	Simulation time (hours)	Simulation time (days)	Speed-up
5 × 5 × 5	10,649	31,947	3114	1	31,947	0.76	0.50	26.08	1.09	1.00
				4	7987	0.76	0.13	6.89	0.29	3.79
				8	3993	0.76	0.08	4.36	0.18	5.99
				16	1997	0.54	0.06	3.20	0.13	8.14
				32	998	0.43	0.05	2.43	0.10	10.71
				64	499	0.32	0.03	1.79	0.07	14.54
10 × 10 × 10	68,921	222,267	4730	1	222,267	11.12	25.41	2002.89	83.45	1.00
				4	55,567	11.12	5.17	407.83	16.99	4.91
				8	27,783	11.12	2.95	232.30	9.68	8.62
				16	13,892	7.97	1.92	151.62	6.32	13.21
				32	6946	7.16	1.38	108.79	4.53	18.41
				64	3473	5.89	0.92	72.26	3.01	27.72
15 × 15 × 15	226,981	714,987	7185	1	714,987	55.07	238.50	28,558.86	1189.95	1.00
				4	178,747	55.07	152.22	18,226.98	759.46	1.57
				8	89,373	55.07	139.62	16,718.21	696.59	1.71
				16	44,687	40.40	31.42	3761.95	156.75	7.59
				32	22,343	38.37	22.45	2688.24	112.01	10.62
				64	11,172	31.14	13.23	1584.61	66.03	18.02

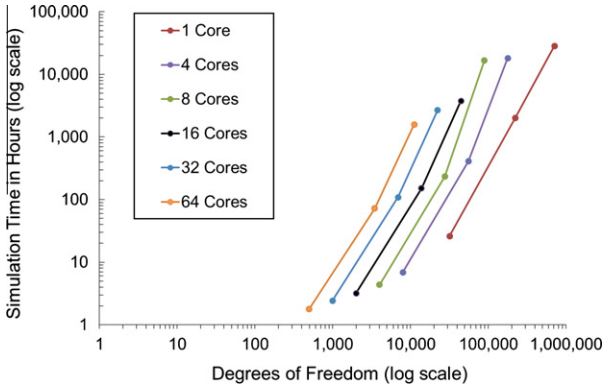

Fig. A2. Simulation time vs. degrees of freedom, illustrating a power-law relationship between variables.

- When scaling the FEM simulations over multiple nodes, speed-up can be maximized by choosing the appropriate number of nodes to ensure the simulation runs within available system memory and to avoid inefficiencies due to excessive internodal communication.
- The microstructure-sensitive FEM captures the measured stressstrain response of subsolvus IN100 at 650 °C reasonably well.
- Future research is needed to better define the minimum number of simulations to build up representative statistics and the minimum allowable statistical volume element size.

Acknowledgments

This work was funded by the National Science Foundation (NSF) Industry/University Cooperative Research Center for Computational Materials Design (CCMD) supported by CCMD members, through Grants NSF IIP-0541674 (Penn State) and IIP-541678 (Georgia Tech). The research was also supported in part by the National Science Foundation through TeraGrid resources provided by The National Center for Supercomputing Applications (NCSA), under grant no. TG-MSS090045. The authors would like to specifically acknowledge the assistance of Dr. Seid Koric for help in running ABAQUS at NCSA. Additionally, we recognize Dr. Michael Groeber and Dr. Michael Uchic of the Air Force Research Lab for providing the reconstructed IN100 dataset and Paul Reynolds and Robert Grelotti at Pratt & Whitney for supplying the experimental IN100 stress–strain data.

Appendix A. Benchmark results

Benchmark results plotted in Fig. A1 and Table A1 were obtained with ABAQUS [28] utilizing the direct solver. They are plotted for a distributed memory cluster consisting of Dell PowerEdge 1955 blades configured with dual socket Intel 64-bit 2.33 GHz processors. Each node contains 8 cores, 16 GB memory, and utilizes InfiniBand interconnects and a Lustre filesystem. The simulations scaled well to 64 cores on both distributed and shared memory systems.

Speed-up is a useful metric to measure the efficacy of utilizing additional processor cores during a finite-element simulation. It can be calculated by dividing the time required to run the simulation with only a single core by the time required to run the same simulation using multiple cores. The 10 × 10 × 10 μm^3 dataset (red line) in Fig. A1 exhibited the highest speed-up value of 27.72 when paired with 64 cores. Speed-up values of 14.54× and 18.02× were reported for the 5 × 5 × 5 μm^3 (blue line) and 15 × 15 × 15 μm^3 (green plot) datasets, respectively. Close examina-

tion of the model size and memory requirements per node in Table A1 helps to explain the results. The amount of system memory available becomes crucial as the model size increases. Both the $5 \times 5 \times 5\ \mu m^3$ and $10 \times 10 \times 10\ \mu m^3$ models required less than 12 GB of memory and therefore ran within system memory. The $15 \times 15 \times 15\ \mu m^3$ simulation, on the other hand, was too large to fit into system memory and thus suffered from inefficient read/write operations. This is evident in Fig. A1, with speed-up times being minimal until scaled over multiple nodes. With 4 nodes (32 cores), the $15 \times 15 \times 15\ \mu m^3$ and $5 \times 5 \times 5\ \mu m^3$ SVEs have equivalent speed-up rates and even with 8 nodes (64 cores), the $15 \times 15 \times 15\ \mu m^3$ dataset requires 31.14 GB of memory to run within memory.

Mesh size can also impact simulation performance. For example, the $21 \times 21 \times 21$ mesh ($5 \times 5 \times 5\ \mu m^3$) did not scale as well as the $41 \times 41 \times 41$ mesh ($10 \times 10 \times 10\ \mu m^3$), even though system memory requirements were lower. This can be explained by inefficiencies in the process. For example, when run over 8 nodes (64 cores), the iteration time for the $5 \times 5 \times 5\ \mu m^3$ dataset was only 2 s. This high rate of simulation time resulted in a larger portion of time being spent in internodal communication as opposed to computation. As a result, the overall efficiency and speed-up ratios of the simulation declined.

Fig. A2 represents a plot of simulation time vs. degrees of freedom on a log–log scale for 1, 4, 8, 16, 32 and 64 cores. The linear nature of the plots suggests a power-law relationship between simulation time and degrees of freedom. This trend can be explained by considering the procedure ABAQUS uses to solve equilibrium equations. ABAQUS employs Newton's method as a numerical technique for solving non-linear equilibrium equations [28]. Although the Newton–Raphson method is reliable and exhibits quadratic convergence, it is often avoided for large finite-element models. This is due to the fact that the expense of forming and solving the complete Jacobian matrix becomes greater as the model size increases [28]. Additionally, the process of forming and solving the Jacobian matrix must be repeated at each iteration step of the analysis. Thus, the power-law relationship between the degrees of freedom and the simulation time can be understood in the context of the nonlinear scaling displayed by ABAQUS when forming and solving the Jacobian matrix. Consequently, the simulation time scales as the square root of the degrees of freedom in the simulation, as illustrated in Fig. A2.

References

[1] McDowell DL, Panchal J, Choi HJ, Seepersad C, Allen J, Mistree F. Integrated design of multiscale, multifunctional materials and products. Boston (MA): Butterworth-Heinemann; 2009.
[2] McDowell D, Olson G. Sci Model Simulat 2008;15:207.
[3] Chen L-Q, Yang W. Phys Rev B 1994;50:15752.
[4] Krill Iii CE, Chen LQ. Acta Mater 2002;50:3059.
[5] Wang AJ, Kumar RS, Shenoy MM, McDowell DL. Int J Multiscale Comput Eng 2006;4:663.
[6] Shenoy MM, Gordon AP, McDowell DL, Neu RW. J Eng Mater Technol 2005;127:325.
[7] Shenoy M, Tjiptowidjojo Y, McDowell D. Int J Plast 2008;24:1694.
[8] Adams BL, Wright SI, Kunze K. Metall Trans A 1993;24:819.
[9] Uchic MD, Holzer L, Inkson BJ, Principe EL, Munroe P. MRS Bull 2007;32:408.
[10] Spanos G, Rowenhorst DJ, Lewis AC, Geltmacher AB. MRS Bull 2008;33:597.
[11] Buffiere J-Y, Cloetens P, Ludwig W, Maire E, Salvo L. MRS Bull 2008;33:611.
[12] Poulsen HF. Three-dimensional X-ray diffraction microscopy: mapping polycrystals and their dynamics. Berlin: Springer Verlag; 2004.
[13] Fan D, Chen LQ. Acta Mater 1997;45:611.
[14] Fan D, Geng C, Chen L-Q. Acta Mater 1997;45:1115.
[15] Chang K, Feng W, Chen L-Q. Acta Mater 2009;57:5229.
[16] Zhu JZ, Wang T, Ardell AJ, Zhou SH, Liu ZK, Chen LQ. Acta Mater 2004;52:2837.
[17] Svoboda J, Fischer FD, McDowell DL. Acta Mater 2012;60:396.
[18] Svoboda J, Fischer FD. Scripta Mater 2010;62:754.
[19] Vedantam S, Patnaik BSV. Phys Rev E 2006;73:016703.
[20] Przybyla CP, McDowell DL. Int J Plast 2010;26:372.
[21] Chaboche JL. Int J Plast 1989;5:247.
[22] Paidar V, Pope DP, Vitek V. Acta Metall 1984;32:435.
[23] Vitek V, Pope DP, Bassani JL. Anomalous yield behaviour of compounds with LI2 structure. In: Nabarro FRN, Duesbery MS, editors. Dislocations in solids, vol. 10. Amsterdam: Elsevier; 1996. p. 135–6 [chapter 51].
[24] Qin Q, Bassani JL. J Mech Phys Solids 1992;40:813.
[25] Qin Q, Bassani JL. J Mech Phys Solids 1992;40:835.
[26] Mecking H, Kocks UF. Acta Metall 1981;29:1865.
[27] Estrin Y, Mecking H. Acta Metall 1984;32:57.
[28] ABAQUS, Version 6.9-EF1. Providence (RI): Simulia; 2009.
[29] Wusatowska-Sarnek AM, Blackburn MJ, Aindow M. Mater Sci Eng: A 2003;360:390.
[30] Wusatowska-Sarnek AM, Ghosh G, Olson GB, Blackburn MJ, Aindow M. J Mater Res 2003;18:2653.
[31] Groeber M, Ghosh S, Uchic MD, Dimiduk DM. Acta Mater 2008;56:1257.
[32] E112-10. Standard test methods for determining average grain size. West Conshohocken (PA): ASTM International; 2010.
[33] OIM Analysis, Version 5.3 Users manual. Mahwah (NJ): Edax, Inc.; 2007.
[34] Kong M, Bhattacharya RN, James C, Basu A. Geol Soc Am Bull 2005;117:244.
[35] MATLAB, Version 7.10. Natick (MA): The MathWorks Inc.; 2010.
[36] Scott DW. Biometrika 1979;66:605.
[37] Vaz MF, Fortes MA. Scripta Metall 1988;22:35.
[38] Wang C, Liu G, Wang G, Xue W. Mater Lett 2007;61:4262.
[39] Bachmann F, Hielscher R, Schaeben H. Solid State Phenom 2010;160:63.
[40] Ostoja-Starzewski M, Sheng PY, Jasiuk I. J Eng Mater Technol 1994;116:384.
[41] Smit RJM, Brekelmans WAM, Meijer HEH. Comput Methods Appl Mech Eng 1998;155:181.
[42] van der Sluis O, Schreurs PJG, Brekelmans WAM, Meijer HEH. Mech Mater 2000;32:449.
[43] Kumar RS, Wang AJ, McDowell DL. Int J Fract 2006;137:173.
[44] Shenoy M, Zhang J, McDowell DL. Fatigue Fract Eng Mater Struct 2007;30:889.
[45] McDowell DL, Berard J-Y. Fatigue Fract Eng Mater Struct 1992;15:719.
[46] Milligan W, Orth E, Schirra J, Savage M. Effects of microstructure on the high temperature constitutive behavior of IN100. In: Green K, Pollock T, Harada H, Howson T, Reed R, Schirra J, Walston S, editors. Superalloys 2004: proceedings of the tenth international symposium on superalloys. Warrendale (PA): TMS; 2004. p. 331.
[47] Rohrer G. JOM J Miner Metals Mater Soc 2007;59:38.

[48] Rohrer GS, Li J, Lee S, Rollett AD, Groeber M, Uchic MD. Mater Sci Technol 2010;26:661.
[49] Dingley DJ, Wilkinson AJ, Meaden G, Karamched PS. J Electron Microsc 2010;59:S155.
[50] Gardner CJ, Kacher J, Basinger J, Adams BL, Oztop MS, Kysar JW. Exp Mech 2011;51:1379.
[51] Adams BL, Kacher J. Comput Mater Continua 2009;14:185.
[52] McDowell DL. Int J Plast 2010;26:1280.
[53] McDowell DL. Mater Sci Eng: R: Rep 2008;62:67.
[54] Fullwood DT, Niezgoda SR, Adams BL, Kalidindi SR. Prog Mater Sci 2010;55:477.
[55] Niezgoda SR, Turner DM, Fullwood DT, Kalidindi SR. Acta Mater 2010;58:4432.
[56] McDowell D, Ghosh S, Kalidindi S. JOM J Miner Metals Mater Soc 2011;63:45.
[57] Lewis AC, Geltmacher AB. Scr Mater 2006;55:81.
[58] Garmestani H, Lin S, Adams BL, Ahzi S. J Mech Phys Solids 2001;49:589.
[59] Ahmadi S. A new Eulerian-based double continuity model for predicting the evolution of pair correlation statistics under large plastic deformations. Brigham Young University, Department of Mechanical Engineering; 2010. p. 174.
[60] Kalidindi SR, Niezgoda SR, Landi G, Vachhani S, Fast T. Comput Mater Continua 2010;17:103.
[61] Fast T, Niezgoda SR, Kalidindi SR. Acta Mater 2011;59:699.
[62] Landi G, Niezgoda SR, Kalidindi SR. Acta Mater 2010;58:2716.